Single and coupled L3 photonic crystal cavities for cavity-QED experiments

Cristian Bonato[a], Jenna Hagemeier [b], Dario Gerace [c], Susanna M. Thon[b, d], Hyochul Kim [b, e], Gareth Beirne[a], Morten Bakker[a], Lucio C. Andreani[c], Pierre M. Petroff[b], Martin P. van Exter[a] and Dirk Bouwmeester[a, b]

[a]Huygens Laboratory, Leiden Institute of Physics, Leiden, the Netherlands;
[b]University of California Santa Barbara, Santa Barbara (CA), USA
[c]Dipartimento di Fisica, Universitá di Pavia, Italy [d] Current Address: Department of Electrical and Computer Engineering, University of Toronto, 10 King's College Road, Toronto, Ontario M5S 3G4, Canada
[e] Department of ECE, IREAP, University of Maryland, College Park, Maryland 20742, USA

ABSTRACT

Here we discuss the experimental characterization of the spatial far-field profiles for the confined modes in a photonic crystal cavity of the L3 type, finding a good agreement with FDTD simulations. We then link the far-field profiles to relevant features of the cavity mode near-fields, using a simple Fabry-Perot resonator model. Finally, we describe a technique for independent all-electrical control of the wavelength of quantum dots in separated L3 cavities, coupled by a waveguide, by electrical isolation via proton implantation

Keywords: photonic crystal cavities, cavity-QED

1. INTRODUCTION

Two-dimensional photonic crystal (PhC) nanocavities in a planar waveguide have found applications in different fields such as nanolasers, nonlinear optics and quantum information processing.[1, 2] Like other resonators, they are essentially characterized by two figures of merit: the cavity quality factor, Q, and the effective confinement volume of each mode, V_{mode}.[3] The quality factor is proportional to the photon lifetime in the cavity which depends on the cavity losses to the external world. The mode volume is a quantitative measure of the spatial confinement of the electromagnetic mode. In most applications, it is crucial to maximize the Q/V_{mode} ratio. For example, the Purcell factor, which measures the enhancement of the spontaneous emission rates for atoms resonant with a cavity is directly proportional to this latter figure of merit. In PhC nanocavities the mode is strongly confined to a very small volume, on the order of $(\lambda/n)^3$, where λ is the mode wavelength. In a planar membrane nanocavity, in-plane confinement is provided by spatial localization on a structural defect in a perfectly periodic PhC with photonic band-gap, while out-of-plane confinement is given by total internal reflection between the slab and the air cladding (assuming a suspended membrane as a planar waveguide). Very high quality factors, in the range 10^4-10^6 have been demonstrated.[4–6] In particular, the L3-type, consisting of three missing holes in a triangular lattice, was the first PhC cavity to show quality factors larger than 10^4.[4]

Here we discuss two topics related to L3 PhC cavities. In Section II, we address the experimental characterization of the far-field of the two modes of L3 cavities, linking properties of the far-field profiles to device parameters via a simplified Fabry-Perot model. In Section III, we focus on a system of two L3 cavities coupled by a waveguide, demonstrating that it is possible to voltage-tune the quantum dots in each cavity independently from one another by electrically isolating the two sample areas via proton implantation.

Further author information: (Send correspondence to Cristian Bonato)
Cristian Bonato: E-mail: bonato@physics.leidenuniv.nl
Dirk Bouwmeester: E-mail: bouwmeester@physics.leidenuniv.nl

2. FAR-FIELD OF PHOTONIC CRYSTAL CAVITY MODES

Most experiments coupling single quantum dot emitters to a nanocavity exploit the lowest-energy mode.[7,8] However, higher order modes can still be important for efficient pumping in nanocavity lasers,[9] selective excitation of quantum dots embedded within the cavity,[10,11] or mutually coupling quantum dots in different spatial positions.[12] The spectral mode structure for L3 cavities has been investigated by Chalcraft and coworkers[13] who compared the calculated resonant energies, quality factors and emission polarizations for the lowest-order modes with experimental data.

Here we report an experimental and theoretical investigation of the spatial far-field profile of the out-of-plane emission for the two lowest-order modes of L3-type PhC nanocavities. The characterization of the out-of-plane far-field emission for PhCs is extremely important for single-photon source applications, since the emitted radiation must be efficiently collected into a fiber. Moreover, in cavity-QED applications, like the ones based on dipole-induced reflection in the one-dimensional atom approximation, mode-matching to an external optical field is crucial.[14,15] Therefore, quite some research has been recently devoted to get a beam-like vertical emission from PhC nanocavities[16–19] for the fundamental mode. Here we extend previous works by analyzing the far-field emission properties of both the fundamental and the second-order mode, introducing a simple model to estimate the essential far-field characteristics of a given near-field mode profile.

We investigated a sample consisting of a 180 nm GaAs membrane grown by molecular beam epitaxy on top of a 0.92 μm $Al_{0.7}Ga_{0.3}As$ sacrificial layer on a GaAs substrate. An $In_{0.4}Ga_{0.6}As$ quantum dot layer is grown at the center of the GaAs membrane by depositing 10 periods of 0.55 Å-thick InAs and 1.2 Å-thick $In_{0.13}Ga_{0.87}As$. The L3 PhC cavities were fabricated on the sample using standard electron beam lithography and reactive ion etching techniques.[20,21] The lattice constant of the triangular hole lattice is $a = 240$ nm. The L3 cavity design was modified for Q optimization (see modified holes in Fig. **??**).[22,23] According to theoretical predictions based on a guided-mode expansion method,[24] the cavity supports two confined modes, with resonances respectively at $\lambda_1^{(th)} = 987$ nm (theoretical Q-factor $Q_{th} \sim 180000$) and $\lambda_2^{(th)} = 957$ nm ($Q_{th} \sim 15000$). Experimentally, we measured the first-order mode with a Lorentzian profile centered around $\lambda_1 = 982.5$ nm and full-width at half-maximum (FWHM) 0.195 ± 0.002 nm, hence an experimental Q-factor $Q \sim 5000$. On the other hand, the second-order mode has a less perfect Lorentzian lineshape centered around $\lambda_2 = 956.4$ nm with FWHM 0.63 ± 0.03 nm, and an experimental Q-factor $Q \sim 1500$. Experimental quality factors are lower then the predicted ones due to scattering from fabrication imperfections[25] and possible absorption from sub-bandgap trap levels and surface states.[26]

The sample was placed in a He-flow cryostat at about 5 K and illuminated above the GaAs bandgap with a few mW laser beam (wavelength 780 nm) on a few μm^2 spot. The photoluminescence from the quantum dot layer embedded in the membrane was collected in the direction normal to the membrane using a microscope objective with numerical aperture $NA = 0.8$ and spectrally analyzed with a spectrometer (resolution 5.5 GHz/pixel). To perform a direct measurement of the far-field emitted intensity at each resonant mode frequency, the filtered photoluminescence at the back focal plane of the microscope objective is imaged. Given a characteristic size of the near-field emission, $a \sim 500$ nm, at a wavelength $\lambda \sim 1$ μm the Fresnel number is $F = a^2/(L\lambda) \sim 0.01$, well in the far-field regime ($L \sim 2$ mm). The far-field was imaged on an intensified CCD camera by a lens with focal length 40 cm in a $2f - 2f$ configuration. To make sure that we were looking at the microscope objective back focal plane, we adjusted the lens to see the sharp image of the objective edge on the CCD. This sharp edge was used to calibrate the numerical aperture scale of the far-field images, assuming that the sharp edges correspond to the $NA = 0.8$ of the objective employed. An interference filter (bandwidth 1 nm) was used to spectrally select the mode of interest. Images were collected after integrating for 30 s and the background noise was removed by subtracting an image taken with a slightly tilted interference filter.

The experimental far-field spatial emission profiles for the first-order and second-order modes are shown in the two larger plots on the bottom side of Fig. 1, together with the far-field projections obtained from FDTD simulations (smaller insets) using the procedure introduced by Vuckovic et al.[27] The first-order mode exhibits a centrally illuminated area extending to about $NA \sim 0.5$, with a ring-like structure inside ($NA \sim 0.2$), matching the low-NA portion of the simulated far-field. The simulated far-field suggests that most of the light from the first-order mode is emitted in two high-NA lobes, which are not collected at all by our set-up. The far-field
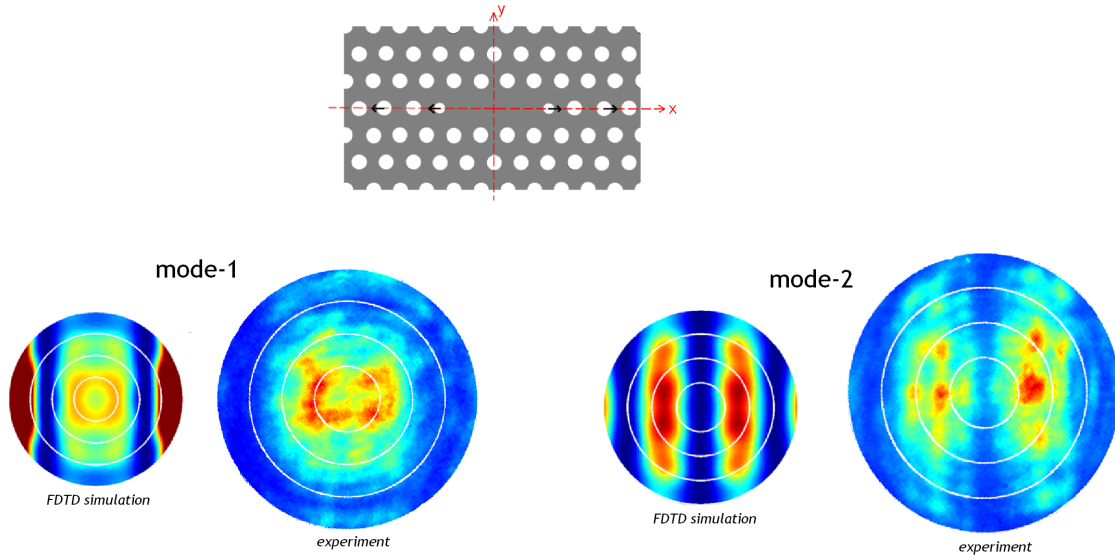
Figure 1. Top: sketch of the L3 photonic crystal cavity used in the experiments. Given a design radius R for the holes, the two holes closest to and in-line with the cavity have reduced design radii $R' = 0.75R$.[22] The small holes are shifted from their lattice positions out from the center of the cavity by a fixed quantity (55 nm). Finally, the third holes (i.e. two holes away from the small holes) are shifted from their lattice positions out from the center of the cavity by 45 nm,[23] to further increase the theoretical Q. Bottom: experimentally measured far-field profiles for the two cavity modes and comparison with the corresponding FDTD simulations.

profile for the second-order mode consists of two lobes, whose center is at a minimal $NA \sim 0.3$.

3D FDTD simulations can predict the far-field emission properties of PhC cavity modes with quite high accuracy. However, they give little physical insight on how the detected features of such far-field profiles can be related to specific device parameters. Here we will show that the essential features of the experimental data can be reproduced by a simple model, elaborated from the proposal of Sauvan and coworkers.[28] For a line of $N \geq 3$ missing holes, the PhC nanocavity can be described quite accurately by a Fabry-Perot resonator, in which the fundamental Bloch mode of a single-line-defect PhC waveguide is trapped between two PhC mirrors of modal reflectivity $r(\lambda)$. The properties of such a cavity are shown to depend only on three parameters, namely the group index n_g of the Bloch mode, the reflection coefficient $r(\lambda)$ of the mirrors and the effective cavity length L.

Let us consider a one-dimensional Fabry-Perot resonator, with the field intensity profile varying sinusoidally in the cavity region and exponentially decaying in the mirror regions, with characteristic penetration depth δ. The far-field profile can be obtained from the near-field using the procedure introduced by Vuckovic and coworkers.[27] According to the surface equivalence theorem, all the information about the far-field profile can be obtained from equivalent electric and magnetic currents, $\mathbf{J}_s = \mathbf{n} \times \mathbf{H}$ and $\mathbf{M}_s = -\mathbf{n} \times \mathbf{E}$, which depend on the in-plane near field components:

$$\begin{array}{ll} N_x = -FT_2(H_y) & N_y = FT_2(H_x) \\ L_x = FT_2(E_y) & L_y = -FT_2(E_x) \end{array} \tag{1}$$

where FT_2 denoted the two-dimensional Fourier transform. These equivalent currents are used to calculate the retarded vector potential of the electromagnetic field, which in the far-field can be related to Fourier transforms of the near-fields. The radiation intensity per unit solid angle can be calculated as:

$$K(\theta, \varphi) = \frac{\eta}{8\lambda^2} \left(\left| N_\theta + \frac{L_\varphi}{\eta} \right|^2 + \left| N_\varphi - \frac{L_\theta}{\eta} \right|^2 \right) \tag{2}$$

where $\eta = \sqrt{\mu_0/\varepsilon_0}$ is the impedance of free-space and λ is the mode wavelength. The radiation vectors in
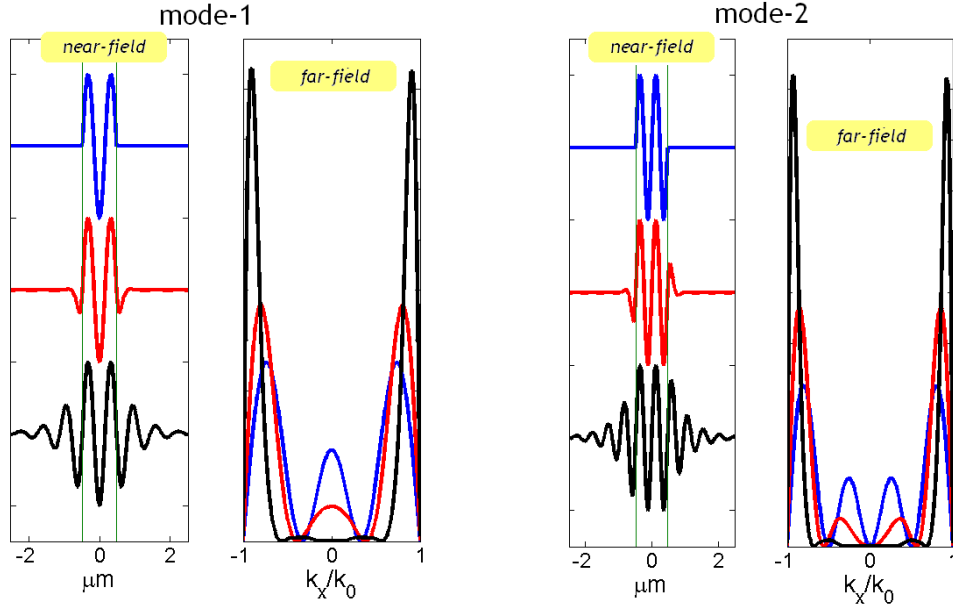
Figure 2. Far-field results for the one-dimensional Fabry-Perot model (first and second-order modes). On the left side, expected near-field profile considering a Fabry-Perot cavity with DBR mirrors with varying penetration depth δ. On the right side, corresponding far-field profiles calculated from Eq. 4. For the first-order mode, in the region $|k_x|/k_0 < 0.5$, there is a single peak centered at $k_x/k_0 = 0$ for small penetration depth. This peak flattens and broadens on increasing penetration depth. For large enough penetration depth, the central peak splits into two smaller peaks. The second-order mode, in the region $|k_x|/k_0 < 0.5$, consists of two peaks that split further and further out for increasing penetration depth δ.

spherical coordinates can be expressed from their cartesian components as:

$$
\begin{aligned}
N_\theta &= (N_x \cos\varphi + N_y \sin\varphi)\cos\theta \\
N_\varphi &= -N_x \sin\varphi + N_y \cos\varphi \ ,
\end{aligned}
\tag{3}
$$

and similarly for **L**. For simplicity, here we consider just the electric field components, so that only L_x is relevant in Eq. 2. Let's consider a separable electric field distribution $E_y(x, y) = \alpha(x)\beta(y)$. The component L_x is separable as well: $L_x = \tilde{\alpha}(k_x)\tilde{\beta}(k_y)$, where $\tilde{\alpha}$ and $\tilde{\beta}$ are the one-dimensional Fourier transforms of $\alpha(x)$ and $\beta(y)$, making:

$$
\begin{aligned}
K(\theta, \varphi) &\propto |\tilde{\alpha}(k_0 \sin\theta \cos\varphi)|^2 |\tilde{\beta}(k_0 \sin\theta \sin\varphi)|^2 \times \\
&\times (\cos^2\varphi \cos^2\theta + \sin^2\varphi)
\end{aligned}
\tag{4}
$$

In a simplified one-dimensional model, $\beta(y)$ is narrow in real-space, so its Fourier transform is wide and can be neglected ($|\tilde{\beta}(k_y)|^2 \sim 1$). If we look at the far-field distribution along the x-axis we select $\varphi = 0$, so that the resulting one-dimensional far-field profile is:

$$
K(\theta) \sim |\tilde{\alpha}(k_0 \sin\theta)|^2 \cos^2\theta
\tag{5}
$$

or, in terms of transverse wavevectors: $K(k_x) \sim |\tilde{\alpha}(k_x)|^2 (k_0^2 - k_x^2)$.

The resonance frequency for the modes can be found setting the condition that the total phase acquired by the Bloch mode traveling back and forth is a multiple of π ($2k_m L = m\pi$), which results in:

$$
k_m = \frac{m\pi}{2L}
\tag{6}
$$

Let us start with a perfectly confined mode, with no penetration into the mirrors ($\delta = 0$). In this case the field is given by:

$$
\alpha_{\delta=0}(x) = \Pi\left(\frac{x}{L}\right) e^{i(k_m x + \phi_m)} + \text{c. c.}
\tag{7}
$$

where $\Pi(x)$ is the rectangular function, $\Pi(x) = 1$ for $|x| < 1/2$ and zero elsewhere. The phase ϕ_m is set by the boundary conditions: $\phi_m = 0$ for m even (cosine-like solutions) and $\phi_m = \pi/2$ for m odd (sine-like solutions). From Eq. 4:

$$K_1(\theta) \quad \sim \left| e^{i\phi_m} \text{Sinc} \left[\frac{m\pi}{2} \left(\sin\theta - 1 \right) \right] + \right.$$
$$\left. + e^{-i\phi_m} \text{ Sinc} \left[\frac{m\pi}{2} \left(\sin\theta + 1 \right) \right] \right|^2 \cos^2\theta \tag{8}$$

Including the penetration depth δ into the model, a simple near-field profile can be taken as a superposition of $\Pi\left(\frac{x}{L}\right)$ and two exponentially-decaying wings, as follows:

$$\alpha(x) \quad = \left[\Pi\left(\frac{x}{L}\right) + H\left(x - \frac{L}{2}\right) e^{-(x-L/2)/\delta} + \right.$$
$$\left. + H\left(-x - \frac{L}{2}\right) e^{-(-x-L/2)/\delta} \right] e^{i(k_m x + \phi_m)} + \text{c. c.} \tag{9}$$

where $H(x)$ is the Heaviside function ($H(x) = 1$ for $x > 0$, $H(x) = 0$ for $x < 0$). The part around $x = 0$ ($\Pi\left(\frac{x}{L}\right)$) gives the same Fourier-transform as in Eq. 8 (which we label $\tilde{\alpha}_1(\sin\theta)$)), while the left and right-side exponential decay regions give the following:

$$\tilde{\alpha}_2(\sin\theta) \quad \sim \quad e^{i\phi_m} \frac{e^{im(\pi/2)(\sin\theta+1)}}{\delta/L - im\pi(\sin\theta+1)} + e^{-i\phi_m} \frac{e^{im(\pi/2)(\sin\theta-1)}}{\delta/L - im\pi(\sin\theta-1)}$$

$$\tilde{\alpha}_3(\sin\theta) \quad \sim \quad e^{i\phi_m} \frac{e^{-im(\pi/2)(\sin\theta\pm1)}}{\delta/L + im\pi(\sin\theta\pm1)} + e^{-i\phi_m} \frac{e^{-im(\pi/2)(\sin\theta-1)}}{\delta/L + im\pi(\sin\theta-1)} \tag{10}$$

All the quantities depend on the ratio δ/L between the penetration depth and the cavity length. The far-field profile can be calculated to be:

$$K_1(\theta) = \left| \sum_{j=1}^{3} \tilde{\alpha}_j(\sin\theta) \right|^2 \cos^2\theta \tag{11}$$

Fig. 2 shows the expected far-field profiles for the first and second-order modes for different values of the penetration depth, δ. The first-order mode exhibits a central peak (centered at $k = 0$) and two outer lobes as predicted by the FDTD simulations. We see that, for increasing penetration depth, the two main outer lobes become narrower in k-space and more outward, while the central peak broadens and flattens. A similar behavior can be observed in the second-order mode. Here, the far-field profile is given by two central peaks and two outer lobes, and again, for increasing penetration depth δ the two outer lobes move outwards and become more localized.

3. COUPLED PHOTONIC CRYSTAL CAVITIES

A long-term goal for solid-state cavity-QED would be to combine on a single chip multiple cavities, each one embedding a single emitter, and connect them through waveguides. This would be a basic building block for a scalable quantum information processing architecture, allowing the implementation of multi-atom entangled states via photon manipulation.[29–31] Furthermore, coupled cavity arrays have been proposed as a quantum simulation tool to investigate the dynamics of quantum many-body systems, originally encountered in condensed-matter physics (like the Bose-Hubbard or Heisenberg models).[32, 33] Interesting physics has also been predicted for driven dissipative arrays of few coupled photonic crystal cavities with single-photon nonlinearities[34–37]

Photonic crystals are an ideal platform to implement these kind of experiments because defect cavities can easily be integrated with waveguides in the same planar photonic lattice structure.[38, 39] Because of the large quantum dot ensemble frequency spread of self-assembled InGaAs quantum dots during the growth process, independent frequency control of spatially separated quantum dots in each cavity is a prerequisite for the implementation of any experiment. Currently existing methods designed to independently tune different quantum dots have significant limitations. Temperature tuning via local heating[40] works only for high enough distances between the QDs and, below about 50K dephasing is increased. Lateral electric field tuning of quantum dots in Schottky diode devices has also been studied,[41] but it provides limited QD emission wavelength tuning ranges and does not allow for deterministic charge control of the QD.

Here, we demonstrate an all-electrical mechanism, by implanting protons in a localized area which electrically isolates regions of quantum dots embedded in a diode structure.[42] Ion or proton implantation is used in semiconductor processing as an isolating technique, since it causes free carrier compensation in a doped semiconductor layer through either irradiation-induced damage or chemically-related deep levels.[43] We show that quantum dots in two spatially-separated waveguide-coupled cavities can be tuned independently, and we also demonstrate that the cavities are optically coupled by pumping one and detecting emission in the other. Our tuning mechanism is robust and scalable, and could be used to independently tune quantum dots laterally separated by as little as $3\ \mu m$.

The sample consists of a 180 nm GaAs membrane grown by molecular beam epitaxy on top of a 0.92 μm $Al_{0.7}Ga_{0.3}As$ sacrificial layer on a GaAs substrate. The $In_{0.4}Ga_{0.6}As$ quantum dot layer is grown in the center of the GaAs membrane by depositing 10 periods of 0.55 Å of InAs and 1.2 Å of $In_{0.13}Ga_{0.87}As$. We used a p-i-n diode design by growing doped layers within the membrane: 30 nm thick p-doped $(2 \times 10^{19}/cm^3)$ and n-doped $(2 \times 10^{18}/cm^3)$ GaAs layers are grown as the top and bottom layers of the GaAs membrane, respectively.
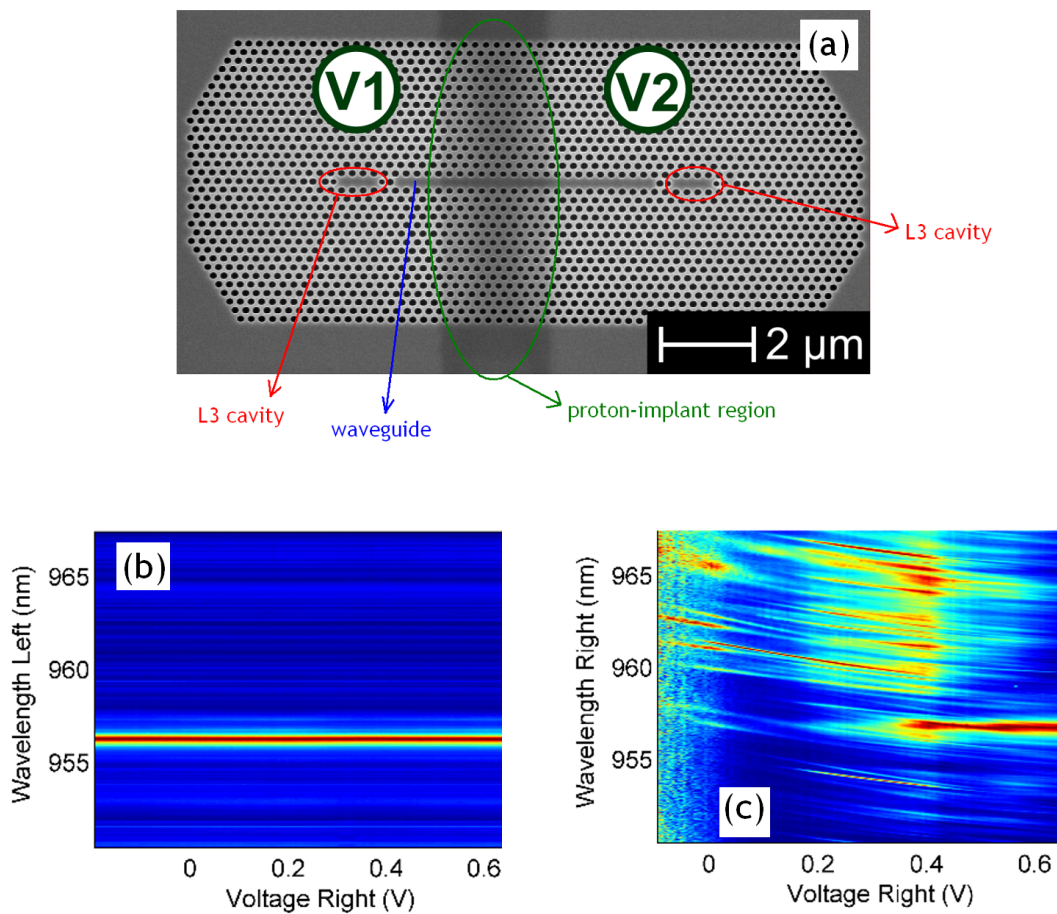

Figure 3. On the top figure, SEM image of the two waveguide-coupled L3 cavities. The darker area perpendicular to the waveguide corresponds to the proton-implanted region. On the bottom row, photoluminescence from the left (b) and right (c) cavities when applying voltage to the right area. No voltage dependence of the photoluminescence can be detected on the left cavity when applying a voltage on the right cavity, due to electrical isolation provided by proton implantation.

Two sets of electrical contacts were fabricated in order to test the proton implant isolation barrier and independent tuning scheme. Because the doped layers are very thin, the sample must be etched to nanometer accuracy to make good electrical contacts to the buried n-doped layer. We use a citric acid/H_2O_2 etch to expose

the n-doped layer. The n-contact metal consists of Ni/AuGe/Ni/Au which is evaporated and annealed. The p-contact metal is evaporated Ti/Pt/Au. After the contacts are defined, we deposit 200 nm of Si_3N_4 on the sample to protect the surface during the proton implant procedure and to maximize the number of protons delivered to the p-doped layer at the specific calculated implant energy. We then perform a final photolithography step to expose the areas in which the proton implant isolating barriers will be created. We defined strips of 1 and 2 μm width in between the two sets of electrical contacts, while the rest of the sample area remained protected by photoresist. To effectively remove the carriers in the p-doped layer, the proton implant dose and energy are calculated using the TRIM (Transport of Ions in Matter) simulator.[44] We performed a proton implantation using a dose of 5×10^{14} cm^{-2} and implant energy of 35 keV in order to electrically isolate the two sets of contacts.

After proton implantation, we fabricated columns of photonic crystal devices across the proton implantation region, using electron beam lithography, followed by reactive ion etching to define the pattern in the membrane and a HF undercut etch to remove the sacrificial layer. The sample layout is shown in Fig. 3a. The photonic crystal devices consist of two L3-type defect cavities separated by approximately 7.5 μm and coupled by a photonic crystal waveguide. The proton implant region cuts through the approximate center of the waveguide in order to electrically isolate the two cavities.

The sample was tested by pumping it with a 780 nm in a flow cryostat and collecting photoluminescence from each of the cavities with a single-mode fiber for spatial selectivity. The output of the single mode fiber was sent through a spectrometer and detected on a CCD. The tuning mechanism was tested by keeping one side of the device at a constant voltage and scanning the voltage across the other side of the device. The results are shown on the bottom of Fig. 3. When the voltage was scanned across the detected cavity, clear Stark shift tuning of the quantum dot emission lines was observed over 2 nm range (right-end side); when the voltage was scanned across the opposite side of the device, the spectrum showed no voltage dependence (left-end side). The same was true for all measured devices, proving that the proton implantation completely isolates electrically the two contact regions.

REFERENCES

1. P. Yao, V. Manga Rao, and S. Hughes, "On-chip single photon sources using planar photonic crystals and single quantum dots," *Laser & Photonics Reviews* **4**, pp. 499–516, 2010.

2. J. L. O'Brien, A. Furusawa, and J. Vuckovic, "Photonic quantum technologies," *Nat Photon* **3**(12), pp. 687–695, 2009.

3. M. Notomi, "Manipulating light with strongly modulated photonic crystals," *Reports on Progress in Physics* **73**(9), p. 096501, 2010.

4. Y. Akahane, T. Asano, B. Song, and S. Noda, "High-Q photonic nanocavity in a two-dimensional photonic crystal," *Nature* **425**(6961), pp. 944–947, 2003.

5. B. Song, S. Noda, T. Asano, and Y. Akahane, "Ultra-high-Q photonic double-heterostructure nanocavity," *Nat Mater* **4**(3), pp. 207–210, 2005.

6. E. Kuramochi, M. Notomi, S. Mitsugi, A. Shinya, T. Tanabe, and T. Watanabe, "Ultrahigh-q photonic crystal nanocavities realized by the local width modulation of a line defect," *Appl. Phys. Lett.* **88**, p. 041112, 2006.

7. S. Strauf, K. Hennessy, M. T. Rakher, Y.-S. Choi, A. Badolato, L. C. Andreani, E. L. Hu, P. M. Petroff, and D. Bouwmeester, "Self-tuned quantum dot gain in photonic crystal lasers," *Physical Review Letters* **96**, p. 127404, 2006.

8. K. Hennessy, A. Badolato, M. Winger, D. Gerace, M. Atatüre, S. Gulde, S. Fält, E. L. Hu, and A. Imamoglu, "Quantum nature of a strongly coupled single quantum dotcavity system," *Nature (London)* **445**, pp. 896–899, 2007.

9. M. Nomura, S. Iwamoto, M. Nishioka, S. Ishida, and Y. Arakawa, "Highly efficient optical pumping of photonic crystal nanocavity lasers using cavity resonant excitation," *Applied Physics Letters* **89**(16), p. 161111, 2006.

10. M. Nomura, S. Iwamoto, T. Yang, S. Ishida, and Y. Arakawa, "Enhancement of light emission from single quantum dot in photonic crystal nanocavity by using cavity resonant excitation," *Applied Physics Letters* **89**(24), p. 241124, 2006.

11. R. Oulton, B. D. Jones, S. Lam, A. R. A. Chalcraft, D. Szymanski, D. O'Brien, T. F. Krauss, D. Sanvitto, A. M. Fox, D. M. Whittaker, M. Hopkinson, and M. S. Skolnick, "Polarized quantum dot emission from photonic crystal nanocavities studied under moderesonant enhanced excitation," *Opt. Express* **15**, pp. 17221–17230, Dec 2007.

12. A. Imamoglu, S. Fält, J. Dreiser, G. Fernandez, M. Atatüre, K. Hennessy, A. Badolato, and D. Gerace, "Coupling quantum dot spins to a photonic crystal nanocavity," *Journal of Applied Physics* **101**(21), p. 081602, 2007.

13. A. R. A. Chalcraft, S. Lam, D. O'Brien, T. F. Krauss, M. Sahin, D. Szymanski, D. Sanvitto, R. Oulton, M. S. Skolnick, A. M. Fox, D. M. Whittaker, H.-Y. Liu, and M. Hopkinson, "Mode structure of the l3 photonic crystal cavity," *Applied Physics Letters* **90**(24), p. 241117, 2007.

14. E. Waks and J. Vuckovic, "Dipole induced transparency in drop-filter cavity-waveguide systems," *Phys. Rev. Lett.* **96**(15), p. 153601, 2006.

15. C. Bonato, F. Haupt, S. S. R. Oemrawsingh, J. Gudat, D. Ding, M. P. van Exter, and D. Bouwmeester, "Cnot and bell-state analysis in the weak-coupling cavity qed regime," *Phys. Rev. Lett.* **104**, p. 160503, Apr 2010.

16. S.-H. Kim, S.-K. Kim, and Y.-H. Lee, "Vertical beaming of wavelength-scale photonic crystal resonators," *Phys. Rev. B* **73**, p. 235117, Jun 2006.

17. N.-V.-Q. Tran, S. Combrié, and A. De Rossi, "Directive emission from high- q photonic crystal cavities through band folding," *Phys. Rev. B* **79**, p. 041101, Jan 2009.

18. M. Toishi, D. Englund, A. Faraon, and J. Vučković, "High-brightness single photon source from a quantum dot in a directional-emission nanocavity," *Opt. Express* **17**, pp. 14618–14626, Aug 2009.

19. S. L. Portalupi, M. Galli, C. Reardon, T. Krauss, L. O'Faolain, L. C. Andreani, and D. Gerace, "Planar photonic crystal cavities with far-field optimization for high coupling efficiency and quality factor," *Opt. Express* **18**, pp. 16064–16073, Jul 2010.

20. A. Badolato, K. Hennessy, M. Atature, J. Dreiser, E. Hu, P. M. Petroff, and A. Imamoglu, "Deterministic coupling of single quantum dots to single nanocavity modes," *Science* **308**(5725), pp. 1158–1161, 2005.

21. S. M. Thon, M. T. Rakher, H. Kim, J. Gudat, W. T. M. Irvine, P. M. Petroff, and D. Bouwmeester, "Strong coupling through optical positioning of a quantum dot in a photonic crystal cavity," *Applied Physics Letters* **94**(11), p. 111115, 2009.

22. L. C. Andreani, D. Gerace, and M. Agio, "Gap maps, diffraction losses, and exciton-polaritons in photonic crystal slabs," *Photonics and Nanostructures - Fundamentals and Applications* **2**, pp. 103 – 110, 2004.

23. Y. Akahane, T. Asano, B.-S. Song, and S. Noda, "Fine-tuned high-q photonic-crystal nanocavity," *Opt. Express* **13**, pp. 1202–1214, Feb 2005.

24. L. C. Andreani and D. Gerace, "Photonic-crystal slabs with a triangular lattice of triangular holes investigated using a guided-mode expansion method," *Phys. Rev. B* **73**, p. 235114, 2006.

25. S. L. Portalupi, M. Galli, M. Belotti, L. C. Andreani, T. F. Krauss, and L. O'Faolain, "Deliberate versus intrinsic disorder in photonic crystal nanocavities investigated by resonant light scattering," *Phys. Rev. B* **84**, p. 045423, Jul 2011.

26. C. P. Michael, K. Srinivasan, T. J. Johnson, O. Painter, K. H. Lee, K. Hennessy, H. Kim, and E. Hu, "Wavelength- and material-dependent absorption in gaas and algaas microcavities," *Applied Physics Letters* **90**(5), p. 051108, 2007.

27. J. Vuckovic, M. Loncar, H. Mabuchi, and A. Scherer, "Optimization of the q factor in photonic crystal microcavities," *IEEE J. Quant. Electr.* **38**, p. 850, 2002.

28. C. Sauvan, P. Lalanne, and J. P. Hugonin, "Slow-wave effect and mode-profile matching in photonic crystal microcavities," *Phys. Rev. B* **71**, p. 165118, Apr 2005.

29. J. Cho and H.-W. Lee, "Generation of atomic cluster states through the cavity input-output process," *Phys. Rev. Lett.* **95**, p. 160501, Oct 2005.

30. J. Cho, D. G. Angelakis, and S. Bose, "Heralded generation of entanglement with coupled cavities," *Phys. Rev. A* **78**, p. 022323, Aug 2008.

31. C. Y. Hu, A. Young, J. L. O'Brien, W. J. Munro, and J. G. Rarity, "Giant optical faraday rotation induced by a single-electron spin in a quantum dot: Applications to entangling remote spins via a single photon," *Phys. Rev. B* **78**, p. 085307, Aug 2008.

32. M. J. Hartmann, F. G. S. L. Brandao, and M. B. Plenio, "Strongly interacting polaritons in coupled arrays of cavities," *Nat Phys* **2**, pp. 849–855, Dec. 2006.

33. M. J. Hartmann, F. G. S. L. Brandao, and M. B. Plenio, "Quantum many-body phenomena in coupled cavity arrays," *Laser & Photon. Rev.* **2**, p. 527, 2008.

34. D. Gerace, H. E. Tureci, A. Imamoglu, V. Giovannetti, and R. Fazio, "The quantum-optical josephson interferometer," *Nat Phys* **5**, pp. 281–284, Apr. 2009.

35. I. Carusotto, D. Gerace, H. E. Tureci, S. De Liberato, C. Ciuti, and A. Imamoğlu, "Fermionized photons in an array of driven dissipative nonlinear cavities," *Phys. Rev. Lett.* **103**, p. 033601, Jul 2009.

36. S. Ferretti, L. C. Andreani, H. E. Türeci, and D. Gerace, "Photon correlations in a two-site nonlinear cavity system under coherent drive and dissipation," *Phys. Rev. A* **82**, p. 013841, Jul 2010.

37. M. Knap, E. Arrigoni, W. von der Linden, and J. H. Cole, "Emission characteristics of laser-driven dissipative coupled-cavity systems," *Phys. Rev. A* **83**, p. 023821, Feb 2011.

38. A. Faraon, I. Fushman, D. Englund, N. Stoltz, P. Petroff, and J. Vučković, "Dipole induced transparency in waveguide coupled photonic crystal cavities," *Opt. Express* **16**(16), p. 12154, 2008.

39. A. Faraon, E. Waks, D. Englund, I. Fushman, and J. Vučković, "Efcient photonic crystal cavity-waveguide couplers," *Appl. Phys. Lett.* **90**, p. 073102, 2007.

40. A. Faraon, D. Englund, I. Fushman, J. Vučković, N. Stoltz, and P. Petroff, "Local quantum dot tuning on photonic crystal chips," *Appl. Phys. Lett.* **90**(21), p. 213110, 2007.

41. A. Faraon, A. Majumdar, D. Englund, E. Kim, M. Bajcsy, and J. Vukovi, "Integrated quantum optical networks based on quantum dots and photonic crystals," *New Journal of Physics* **13**(5), p. 055025, 2011.

42. S. M. Thon, H. Kim, C. Bonato, J. Gudat, J. Hagemeier, P. M. Petroff, and D. Bouwmeester, "Independent electrical tuning of separated quantum dots in coupled photonic crystal cavities," *Applied Physics Letters* **99**(16), p. 161102, 2011.

43. M. Ridgway, R. Elliman, and N. Hauser, "Mev in-ion implantation for electrical isolation of p+-inp," *Nuclear Instruments and Methods in Physics Research Section B: Beam Interactions with Materials and Atoms* **80-81**(Part 2), p. 835, 1993.

44. J. F. Ziegler, J. P. Biersack, and U. Littmark, *The Stopping and Range of Ions in Solids*, Pergamon Press, New York, 1985.